



Repositorio Institucional de la Universidad Autónoma de Madrid

<https://repositorio.uam.es>

Esta es la **versión de autor** del artículo publicado en:

This is an **author produced version** of a paper published in:

Journal of Alloys and Compounds 596 (2014): 140 - 144

DOI: <http://dx.doi.org/10.1016/j.jallcom.2014.01.177>

Copyright: © 2014 Elsevier

El acceso a la versión del editor puede requerir la suscripción del recurso

Access to the published version may require subscription

Disorder and variable-range hopping conductivity in $\text{Cu}_2\text{ZnSnS}_4$ thin films prepared by flash evaporation and post-thermal treatment

M. Guc^a, R Caballero^{b*}, K. G. Lisunov^{a,c}, N. López^b, E. Arushanov^a, J. M. Merino^b, M. León^b

^aInstitute of Applied Physics, Academy of Sciences of Moldova, Academiei Str. 5, MD-2028 Chişinău, Moldova

^bUniversidad Autónoma de Madrid, Departamento de Física Aplicada, C/ Francisco Tomás y Valiente 7, 28049 Madrid, Spain

^cLappeenranta University of Technology, PO Box 20, FIN-53852 Lappeenranta, Finland

*Corresponding author: raquel.caballero@uam.es; +34 91 497 8559

Abstract.

Resistivity, $\rho(T)$, of as-grown and annealed $\text{Cu}_2\text{ZnSnS}_4$ films, obtained by flash evaporation, is investigated between $T \sim 10 - 300$ K. A correlation between the transport properties and the growth conditions of the thin films is also explored. The behavior of $\rho(T)$ in the as-grown films exhibits a close proximity to the metal-insulator transition (MIT), whereas annealing shifts the material from the MIT towards an insulating side. This is attributable to an increased microscopic lattice disorder, which is substantiated by the analysis of the Mott variable-range hopping conductivity observed up to $T \sim 220 - 280$ K (120 – 180 K) in the as-grown (annealed) films. An increased width of the acceptor band, a decreased relative acceptor concentration, N/N_c and lower values of the mean density of the localized states, g , are obtained after annealing.

Keywords: $\text{Cu}_2\text{ZnSnS}_4$, Kesterite, Hopping conductivity, Flash evaporation, Acceptor band, Solar cell.

1. Introduction

The thin film photovoltaic (PV) technologies are based on direct band gap materials, such as CuInSe_2 , $\text{CuIn}_{1-x}\text{Ga}_x\text{Se}_2$ and CdTe . However, due to the toxicity of Cd and Se and the availability issues of In and Te, the large-scale production of the PV devices based on these absorber layers

is limited. $\text{Cu}_2\text{ZnSnS}_4$ (CZTS) is a quaternary compound that has emerged as a promising absorber for thin film solar cells. This material has excellent optical properties, absorption coefficient $\alpha > 10^4 \text{ cm}^{-1}$ and a direct band gap energy that matches well the solar spectrum. Moreover, all the constituents of CZTS are low cost, non-toxic and earth abundant [1-2].

Katagiri et al. reported CZTS-based solar cells over 6.7 % efficiency for the first time. Since then, several groups are making important efforts to enhance the efficiencies of these devices [3]. The highest efficiency reported to date, 12.6 %, was obtained by depositing CZTSSe using a hydrazine-based pure solution approach [4]. An efficiency of 9.2% on $5 \times 5 \text{ cm}^2$ -sized pure CZTS submodule has been achieved by the annealing of metal precursors by Solar Frontier [5]. Other physical and chemical techniques are being currently investigated to prepare CZTS thin films: thermal evaporation and subsequent annealing at atmospheric pressure achieving a performance of 8.4% [6], reactive pulsed dc magnetron co-sputtering of Cu-Zn-Sn-S in an atmosphere of H_2S and subsequent annealing producing a 7.9%-CZTS solar cell [7], electroplating metal stacks converted into CZTS by high temperature sulfurization with a 7.3 % efficiency-device [8], thermal decomposition and reaction using a non-toxic sol-gel route producing 5.1 %-CZTS solar cells [9], single step sputtering, which has been shown as a facile and cost-effective preparation method [10], rapid thermal process of reactively sputtered precursors yielding 4.6 % efficiency for CZTS-devices [11], pulsed laser deposition followed by post-annealing achieving a 4.3 % CZTS-based device [12], etc.

However, the performance of CZTS-based solar cells is still far away from the 20.8 % of the Cu(In,Ga)Se_2 devices. A more intricate understanding of the fundamental properties of the CZTS material is still necessary for the improvement of the solar cells. Among other characteristics, the knowledge of the structure and transport properties of the absorber layer is fundamental for the design of high efficient PV devices. However, only the room-temperature resistivity [13-14] and minority carrier-diffusion length [4] have been determined so far for thin films prepared by different evaporation techniques.

In the present work, the preparation, structural and transport characterization of CZTS thin films grown by the flash evaporation [15-16] and subsequent thermal treatment are reported. Temperature dependence of the resistivity of $p\text{-Cu}_2\text{ZnSnS}_4$ thin films is investigated between $T \sim 10 - 300 \text{ K}$. The purpose of this work is to investigate the conductivity mechanisms as well as

some details of the energy spectrum and other microscopic properties of the charge carriers. A correlation between the transport properties and growth conditions of CZTS films is established.

2. Experimental details

CZTS thin films were deposited by flash evaporation of ZnS, CuS and SnS binary compounds in powder form onto glass substrates at a nominal substrate temperature of 100° C. Salavati-Niasari et al. have synthesized ZnS [17], SnS [18] and Cu₂S [19] nanostructures by chemical methods. In our case, and considering these previous works, CuS and SnS powders were synthesized in an evacuated quartz ampoule from the pure elemental constituents, while commercially available ZnS was used. A preferential re-evaporation of Zn was observed during the flash evaporation process. The same behavior was observed when thin films were deposited by flash evaporation of the pre-synthesized quaternary CZTS compound in powder form. This behavior was related to a preferential Zn re-evaporation due to its high partial vapor pressure [16]. Therefore, a precursor with excess of ZnS was used in our deposition procedure. Fig. 1 summarizes the different deposition processes and the composition of the thin films measured by Energy Dispersive X-ray spectroscopy (EDX) (Oxford instruments, model INCAx-sight) inside a Hitachi S-3000N scanning electron microscope. EDX measurements were carried out at 20 kV operating voltage, and the Cu K, Zn K, Sn L and S K lines were used for quantification. As follows in Table 1, the thin film composition depends on the crucible temperature used during the flash deposition. Lower crucible temperatures led to higher Cu concentrations [16]. Post-thermal treatments of the samples in Ar atmosphere (at pressures of 100 and 1000 Pa) under excess of S were carried out. For that purpose, the as-grown thin films were placed in a partially closed graphite box inserted inside a quartz tube furnace. In order to have an overpressure of S, 20 mg of elemental sulfur were also supplied into the graphite container. Parameters such as maximum temperature, Ar pressure and the heating rate were varied to obtain the CZTS material with the optimum structural and electrical properties. Details of the thermal treatments applied to the samples are also collected in Table 1.

Grazing incidence X-ray diffraction (GIXRD) was performed to investigate the structural properties of the CZTS thin films. GIXRD data were collected with a PaNAlytical X'Pert Pro MPD diffractometer, using the Cu K_α radiation and a multilayer mirror. Detector scans with incident angles of 0.25°, 2° and 4° were carried out. The temperature dependence of the

resistivity, $\rho(T)$, was measured between $T \sim 10 - 300$ K by the Van der Pauw method. To produce the contacts In soldered was used in the case of the annealed films, while In:Ga alloy was used for the as-grown films to avoid the sample heating. The sample was placed in a closed circle helium cryostat to control the temperature. The hot probe method showed that all the investigated thin films had p -type conductivity.

3. Results and discussion

The temperature dependence of the resistivity before and after the thermal treatments of the samples is shown in Fig. 1. The as-grown films exhibit a weakly activated behavior of $\rho(T)$, accompanied with relatively low values of the resistivity. These features imply a close proximity of the material to the metal-insulator transition (MIT) on the insulating side of the MIT. However, as is shown in the middle panel of Fig. 1, the thermal treatment-1 (TT1) shifts the material from the MIT towards the insulating state, increasing the resistivity and the variation of ρ with T .

The proximity of a system to the MIT is strongly influenced by the microscopic lattice disorder [20]. The behavior of $\rho(T)$ in Fig. 1 suggests that thermal treatment TT1 leads, generally, to a lattice disorder increase. This is connected probably to a mix of kesterite and stannite CZTS structures. Indeed, the total energy of both structures is extremely close [21], allowing the generation of a mixed (disordered) phase [21, 22].

Raman spectroscopy has been used to analyze most of the samples [23]. The Raman spectra showed, not only the A-mode peak at $337\text{-}338\text{ cm}^{-1}$, characteristic of the ordered kesterite, but also a weak additional peak at 331 cm^{-1} . This peak at 331 cm^{-1} is associated with the disorder in the cation lattice and with the formation of the Cu_{Zn} and Zn_{Cu} antisites [23].

Nonetheless, thermal treatment TT2 leads to an opposite effect, transforming the activated dependence of $\rho(T)$ into the metallic one (in the bottom panel of Fig. 1). The effect of the thermal treatment TT3 is similar to TT2, but is much weaker. This fact suggests an important role of the Ar pressure during the thermal treatment. As observed in Table 1, the Ar pressure has a significant influence on the composition of the final compound and this is reflected in the dramatic change in the resistivity.

Fig. 2 displays the comparison of GIXRD spectra with $\text{GI} = 4^\circ$ for the thin film S1 before and after the different thermal treatments applied, resulting in S1-1, S1-2 and S1-3 respectively (the

second number refers to the thermal treatment applied). Two important features are observed in these spectra: (i) an enhanced crystalline quality after the annealing and (ii) the presence of Cu_2S for the samples annealed following the TT2 and TT3 treatments, could be a reason for the apparent enhancement of the metallic properties of CZTS, as observed in Fig.1. Indeed, the resistivity down to $\sim 7 \times 10^{-4} \Omega \text{ cm}$, achieved recently in Cu_xS films with $x = 1 - 3$ [24], is much smaller than the one observed in the as-grown samples. Therefore, even a relatively small fraction of the macroscopic inclusions of such phases may reduce the net resistivity of the inhomogeneous system ($\text{CZTS} + \text{Cu}_2\text{S}$) substantially. Such a behavior resembles the shift of the conventional homogeneous semiconductor towards the metallic side of the MIT.

Further information on disorder and valuable microscopic parameters of charge carriers in our samples can be obtained by investigation of the Mott variable-range hopping (VRH) conduction [20, 25]. Such mechanism of the charge transfer has recently been established in CZTS single crystals [26] and films [27-29], as well as in $\text{Cu}_2\text{ZnSiSe}_4$ single crystals [30], belonging to the same family of compounds. The upper border of the VRH conduction in the above materials, lying close to the room temperature, reflects the high lattice disorder [26-30]. Indeed, such disorder stimulates the localization of the conduction electrons, favoring the hopping conductivity [20]. On the other hand, the VRH charge transfer is expectable when the Fermi level, μ , lies close to one of the edges of the impurity band (or the acceptor band (AB) in our case of the *p*-type semiconductor) [25]. This takes place for the cases of a weak ($K \ll 1$) or strong ($1 - K \ll 1$) degree of the compensation, K , as it has been established in [26] and [30], respectively. Following the arguments in [26] and [30], we can assume one of the two cases, considering the proximity to the MIT given by the relatively small difference of $|\mu - E_c|$, where $+E_c$ and $-E_c$ are the mobility edges [20]. Because the impurity states are extended within the $(-E_c, +E_c)$ interval around the center of an impurity band and are localized outside this interval, the position of μ close to one of the AB edges or tails is consistent with the VRH conduction regime [20]. The DOS model discussed above is shown in Fig. 3(a), being used in the subsequent analysis below.

The resistivity governed by the Mott VRH mechanism is given by the expression [20, 25]:

$$\rho(T) = AT^{1/4} \exp \left[\left(\frac{T_0}{T} \right)^{1/4} \right], \quad (1)$$

where A is a prefactor constant, $T_0 = \beta / [k a^3 g(\mu)]$ [14, 19] is the VRH characteristic temperature depending on the localization radius, $a = a_0 (1 - N/N_c)^{-\nu}$ [31], and on the density of the localized states (DOS), $g(\mu)$, at the Fermi level, and $\beta \approx 21$ is a numerical constant [25]. Here N is the concentration of acceptors, N_c is the critical concentration of the MIT, a_0 is the value of a far from the MIT (i. e. at $N \ll N_c$) and $\nu \approx 1$ is the critical exponent [31].

As follows from Eq. (1), the plots of $\ln(\rho T^{-1/4})$ vs. $T^{-1/4}$ in the interval of the Mott VRH conduction should be represented by linear functions. This is consistent with the behavior shown in Fig. 4 within the broad intervals of the temperature given in Table 2 by the upper (T_v) and lower (T_m) borders, yielding the values of T_0 and A collected in Table 2. The semi-width of the AB evaluated with the expression $W \approx 0.5 (T_v^3 T_0)^{1/4}$ [26, 30] is also displayed in Table 2, reflecting the enhanced disorder in the majority of the annealed films, where W exceeds the data of as-grown samples. In the approximation of the DOS with a rectangular shape, $g(\mu) \approx g_{av} \equiv N/(2W)$, is valid [26, 30] in the next equation, yielding the values of the ratio N/N_c collected in Table 2.

$$\left(\frac{T_0}{T_v} \right)^{1/4} \approx 4\beta^{1/3} \left(\frac{N_c}{N} \right)^{1/3} \left(1 - \frac{N}{N_c} \right)^\nu \quad (2)$$

The enhanced values of N/N_c in the as-grown films are consistent with their close proximity to the MIT, which takes place also for the annealed film, S3-1. The values of $N/N_c \sim 0.1$ for samples S1-1 and S2-1 indicate a strong insulating regime of these samples, when the difference of $|\mu - E_c|$ is large or the interval of extended states ($-E_c, +E_c$) in the AB does not exist at all. The broadness of the AB for S1-1 and S2-1 (Table 2), connected to the high lattice disorder, correlates well with the above conclusion, taking into account that the high disorder stimulates considerably the localization of the charge carriers [20]. Because the samples S1-1 and S2-1 cannot be characterized by their close proximity to the MIT, they do not satisfy the conditions assumed above, and the microscopic data of the relative localized carriers cannot be found with the method used below, which has been proposed in [26, 30]. Therefore, the values of the ratio $a/a_0 = (1 - N/N_c)^{-\nu}$ can be calculated only for the rest of investigated CZTS films at $\nu = 1$, as collected in Table 2.

The value of a_0 in doped semiconductors is close to the Bohr radius, a_B [25], where both parameters are given by the expressions

$$a_0 = \hbar(2mE_0)^{-1/2} \quad \text{and} \quad a_B = \hbar^2 \kappa_0 (me^2)^{-1}, \quad (3)$$

respectively [19]. Here, $m \approx 0.47 m_0$ is the mean hole mass of CZTS [21, 26], E_0 is the energy of the DOS peak in the AB (see Fig. 3(a)) and κ_0 is the dielectric permittivity of the material far from the MIT [25]. The ratio of $a/a_B = (1 - E_c/\mu)^{-\nu}$ [20, 25] can be evaluated by putting $\mu \approx W$ and using the expression $E_c \approx W - V_0^2 / [4(z-1)J]$ [17], where $V_0 \approx 2W$ [24, 28] and $J = J_0 \exp(-R/a_B)$ is the overlap integral [20, 25]. Here $R \approx (4\pi N/3)^{-1/3}$ is the half of the mean distance between the acceptors, and J_0 is a prefactor, $J_0 \approx 2e^2 R / (e_1 \kappa_0 a_B^2)$ [25], where $e_1 = \exp(1)$. The only unknown parameter for the evaluation of a/a_B with these expressions is κ_0 , which can be obtained by fitting the values of a/a_0 in Table 2 to those of a/a_B by minimizing the standard deviation (SD) [26, 30]. Such fitting was performed only for the as-grown films using the expression:

$$SD = \left\{ \frac{1}{3} \sum_{i=1}^3 [(a/a_0)_i - (a/a_B)_i]^2 \right\}^{1/2}, \quad (4)$$

where i is the sample number. The best fit yields $\kappa_0 = 8.4$ at $SD = 0.066$, and the values of a/a_B are in a reasonable agreement with those of a/a_0 (see Table 2, lines 1 – 3). Eventually, the values of $E_0 \approx 90$ meV and $a_B \approx 9.5 \text{ \AA}$ are obtained with Eqs. (3), which yields with the universal Mott criterion, $N_c^{1/3} a_B \approx 0.25$ [20], the value of the critical concentration $N_c \approx 1.8 \times 10^{19} \text{ cm}^{-3}$. The data of E_c and $g(\mu)$ can be obtained with the above similar procedure, resulting in the values collected in Table 2.

The corresponding values for the sample S3-1 are obtained by fitting a/a_0 with a/a_B separately, yielding $\kappa_0 \approx 8.45$, $E_0 \approx 89$ meV, $a_B \approx 9.5 \text{ \AA}$ and $N_c \approx 1.9 \times 10^{19} \text{ cm}^{-3}$. The values of E_c and $g(\mu)$ for this sample are given in Table 2. It can be observed that the data of κ_0 , E_0 , a_B and N_c obtained for the annealed sample S3-1 are quite close to those of the as-grown films, S1–S3.

It is worth mentioning that the values of $\kappa_0 = 8.4$ and 8.45 obtained for the samples S1–S3 and S3-1 respectively, are quite close to the data determined from the capacitance spectra of the CZTS thin films ($\kappa_0 \approx 8$) [32] or evaluated with first-principle calculations ($\kappa_0 = 9.1 - 9.7$) [33] in $\text{Cu}_2\text{ZnSnS}_4$. This supports the validity of the microscopic parameter values obtained for these samples and collected in Table 2, being the values of N , E_c , a and $g(\mu)$ in a reasonable

agreement with the corresponding data obtained for CZTS bulk [26] and film [27-29] samples, as well as for $\text{Cu}_2\text{ZnSiSe}_4$ single crystals [30].

Eventually, as can be observed in the inset of the middle panel of Fig. 1, the plot of $\ln \rho$ vs. T^{-1} for the most insulating samples, S1-1 and S2-1, exhibits linear parts within a sufficiently broad temperature interval $\Delta T \sim 200 - 300$ K to be interpreted with the law $\rho = \rho_0 \exp(E_a/kT)$, with $\rho_0 \approx 0.389$ and $0.293 \text{ } \Omega \text{ cm}$, and $E_a \approx 70$ and 71 meV , respectively. Because the values of $E_a \sim 70 \text{ meV}$ are comparable to those of $E_0 \sim 90 \text{ meV}$, obtained above, a conductivity due to thermal activation of the holes from acceptor levels to the valence band is suggested. The difference of $\sim 30 \%$ between E_0 and E_a could be related to two possible reasons. The first reason is the error in the E_0 determination due to the use of the rectangular DOS shape in the analysis of the VRH conduction. However, a good agreement of κ_0 with the literature data indicates that such error should not be too large. The other reason is connected to the high temperatures $\sim 200 - 300 \text{ K}$ used, where the values of E_a have been obtained, and which leads to high enough concentration of the holes in the valence band when screening effects should be important. It is known that screening of impurities by itinerant band carriers reduces the values of the impurity levels [34]. Therefore, the value of E_0 is addressed rather to a situation of $T \rightarrow 0$ and yields the mean energy of unscreened acceptors in CZTS. On the other hand, E_a represents the acceptor energy at finite $T \sim 200 - 300 \text{ K}$, close to the room temperature, when the screening effect is expected to be strong.

Additionally, comparing the values of $W \approx 117 \text{ meV}$ and 140 meV for S1-1 and S2-1 samples (Table 2) and $E_0 \sim 90 \text{ meV}$, it is evident that the AB in S1-1 and S2-1 should overlap with the VB states at $T \rightarrow 0$. At finite temperatures such overlap should be even increased due to a reduction of the acceptor energies by the screening effects discussed above. Therefore, the near-edge band structure of S1-1 and S2-1 is given rather by the plot shown schematically in Fig. 3(b), where the majority of the acceptor states are localized due to the strong disorder, and the position of the single mobility edge, E_c , is close to the edge of unperturbed (or addressed to low disorder) valence band, E_v .

4. Conclusions

The resistivity of as-grown and annealed CZTS films prepared by the flash evaporation method has been studied. The Ar pressure during the thermal treatment is shown as an important parameter to control the composition of the material and, consequently, its electrical properties. The as-grown samples exhibit low resistivity and a weak dependence of ρ with T, addressed to a close proximity of the material to the metal-insulation transition. However, the annealing shifts the material considerably towards the insulating side of the MIT. This can be attributable to the increase of the lattice disorder produced in the majority of the samples. Analysis of the Mott variable-range hopping conduction supports this conjecture, yielding an increase of the width of the acceptor band and a decrease of the acceptor concentration in the annealed CZTS films, typical of the enhanced disorder. The values of the microscopic parameters of the localized carriers, as well as details of the whole spectrum near the edge of the acceptor band are obtained in agreement with the literature data.

Acknowledgments

This research is supported by the People Programme (Marie Curie Actions) of the European Union's Seventh Framework Program FP7/2007-2013/ under REA grant agreement 269167 (PVICOKEST), the Spanish MINECO project (KEST- PV, ENE2010-21541-C03) and FRCFB 13.820.05.11/BF project. RC acknowledges financial support from Spanish MINECO within the program Ramón y Cajal (RYC-2011-08521).

References

- [1] M.P. Suryawanshi, G.L. Agawane., S.M. Bhosale., S.W. Shin., P.S. Patil, J.H. Kim, A.V. Moholkar., *Materials Technology* 28 (2013) 98-109.
- [2] H. Katagiri, *Thin Solid Films* 481 (2005) 426-432. DOI: 10.1016/j.tsf.2004.11.024.
- [3] H. Katagiri, K. Jimbo, S. Yamada, T. Kamimura, W.S. Maw, T. Fukano, T. Ito, T. Motohiro, *Appl. Phys. Express* 1 (2008) 041201 (2 pp). DOI: 10.1143/APEX.1.041201.
- [4] W. Wang, M.T. Winkler, O. Gunawan, T. Gokmen, T.K. Todorov, Y. Zhu, D.B. Mitzi, *Adv. Energy Mater.* 2013, DOI: 10.1002/aenm.201301465.
- [5] T. Kato, H. Hiroi, N. Sakai, S. Muraoka, H. Sugimoto, Characterization of front and back interfaces on $\text{Cu}_2\text{ZnSnS}_4$ thin film solar cells, in: 27th EPSEC, Frankfurt (2012), pp. 2236-2239.

- [6] B. Shin, O. Gunawan, Y. Zhu, N.A. Bojarczuk, S. Jay Chey, S. Guha, *Prog. Photovolt: Res. Appl.* 21 (2013) 72-76. DOI: 10.1002/pip.1174.
- [7] J.J. Scragg, T. Kubart, J.T. Wätjen, T. Ericson, M.K. Linnarsson, Ch. Platzer-Björkman, *Chem. Mater* 25 (2013) 3162-3171. DOI: 10.1021/cm4015223.
- [8] S. Ahmed, K.B. Reuter, O. Gunawan, L. Guo, L.T. Romankiw, H. Deligianni, *Adv. Energy Mater.* 2 (2012) 253-259. DOI: 10.1002/aenm.201100526.
- [9] Z. Su, K. Sun, Z. Han, H. Cui, F. Liu, Y. Lai, J. Li, X. Hao, Y. Liu, M.A. Green, *J. Mater. Chem. A* 2 (2014) 500-509. DOI: 10.1039/C3TA13533K.
- [10] J. Wang, S. Li, J. Cai, B. Shen, Y. Ren, G. Qin, *J. Alloys Compd.* 552 (2013) 418-422. DOI: 10.1016/j.jallcom.2012.11.082.
- [11] J.J. Scragg, T. Ericson, X. Fontané, V. Izquierdo-Roca, A. Pérez-Rodríguez, T. Kubart, M. Edoff, C. Platzer-Björkman, *Prog. Photovolt: Res. Appl.* 22 (2014) 10-17. DOI: 10.1002/pip.2265.
- [12] A.V. Moholkar, S.S. Shinde, G.L. Agawane, S.H. Jo, K.Y. Rajpure, P.S. Patil, C.H. Bhosale, J.H. Kim, *J. Alloys Compd.* 544 (2012) 145-151. DOI: 10.1016/j.jallcom.2012.07.108.
- [13] H. Katagiri, K. Saitoh, T. Washio, H. Shinohara, T. Kurumadani, S. Miyajima, *Sol. Energy Mater. Sol. Cells* 65 (2001) 141-148.
- [14] C. Shi, G. Shi, Z. Chen, P. Yang, M. Yao, *Mater. Letters* 73 (2012) 89-91. DOI: 10.1016/j.matlet.2012.01.018.
- [15] J.M. Merino, M. León, F. Rueda, R. Díaz, *Thin Solid Films* 361-362 (2000) 22-27.
- [16] R. Caballero, V. Izquierdo-Roca, J.M. Merino, E.J. Friedrich, A. Climent-Font, E. Saucedo, A. Pérez-Rodríguez, M. León, *Thin Solid Films* 535 (2013) 62-66. DOI: 10.1016/j.tsf.2012.10.028.
- [17] A. Sobhani, M. Salavati-Niasari, M. Sobhani, *Mater. Science in Semicond. Process.* 16 (2013) 410-417. DOI: 10.1016/j.mssp.2012.09.002.
- [18] M. Salavati-Niasari, D. Ghabari, F. Davar, *J. Alloys Compd.* 492 (2010) 570-575. DOI: 10.1016/j.jallcom.2009.11.183.
- [19] M. Mousavi-Kamazani, M. Salavati-Niasari, M. Sadeghinia, *Superlattices and Microstructures* 63 (2013) 248-257. DOI: 10.1016/j.spmi.2013.08.023.
- [20] N. Mott, E.A. Davies, *Electron Processes in Non-Crystalline Materials*, ed. Clarendon, Oxford, 1979; N.F. Mott, *Metal-Insulator Transitions*, ed. Taylor and Francis, London, 1990.

- [21] C. Persson, J. Appl. Phys. 107 (2010) 053710 (8 pp). DOI: 10.1063/1.3318468.
- [22] S. Schorr, Thin Solid Films 515 (2007) 5985-5991. DOI: 10.1016/j.tsf.2006.12.100.
- [23] R. Caballero, E. Garcia-Llamas, J.M. Merino, M. León, I. Babichuck , V. Dzhagan, V. Strelchuck, M. Valakh, Acta Materialia 65 (2014) 412-417. DOI: 10.1016/j.actamat.2013.11.010.
- [24] J. Santos Cruz , S.A. Mayén Hernández, J.J. Coronel Hernández, R. Mejía Rodríguez, R. Castanedo Pérez G. Torres Delgado, S. Jiménez Sandoval , Chalcogenide Letters 9 (2012) 85-91.
- [25] B.I. Shklovskii , A.L. Efros, Electronic Properties of Doped Semiconductors, ed. Springer, Berlin, 1984.
- [26] K.G. Lisunov, M. Guk, A. Nateprov, S. Levchenko, V. Tezlevan, E. Arushanov, Sol. Energy Mater. Sol. Cells 112 (2013) 127-133. DOI: 10.1016/j.solmat.2013.01.027.
- [27] J.C. González, G.M. Ribeiro, E.R. Viana, P.A. Fernandes, P.M.P. Salomé, K. Gutierrez, A. Abelenda, F.M. Matinaga , J.P. Leitão, A.F. da Cunha, J. Phys. D: Appl. Phys. **46** (2013) 155107 (7 pp). DOI: 10.1088/0022-3727/46/15/155107.
- [28] V. Kosyak, M.A. Karmarkar M A, M.A. Scarpulla, Appl. Phys. Lett. 100 (2012) 263903 (5 pp).
- [29] M.A. Majeed Khan, S. Kumar, M. Alhoshan, A.S. Al Dwayyan, Optics & Laser Technology 49 (2013) 196-201. DOI: 10.1016/j.optlastec.2012.12.012.
- [30] K.G. Lisunov, M. Guc, S. Levchenko, D. Dumcenco, Y.S. Huang, G. Gurieva, S. Schorr, E. Arushanov, J. Alloys Compd. 580 (2013) 481-486. DOI: 10.1016/j.jallcom.2013.06.156.
- [31] T.G. Castner, Hopping conduction in the critical regime approaching the metal–insulator transition, in: M. Pollak, B. Shklovskii (Eds.), Hopping Transport in Solids, North-Holland, Amsterdam, pp. 1–49. 1251991; K. Lisunov , E. Arushanov, Ch. Kloc, U. Malang, E. Bucher, Phys. Stat. Sol. b 195 (1996) 227-236. DOI: 10.1002/pssb.2221950125.
- [32] O. Gunavan, T. Gokmen, C.W. Warren , J.D. Kohen, T.K. Todorov, D.A.R. Barkhouse, S. Bag, J. Tang, B. Shin, D.B. Mitzi, Appl. Phys. Lett. 100 (2012) 253905 (4 pp).
- [33] J. Paier, R. Asahi, A. Nagoya, G. Kresse, Phys. Rev. B 79 (2009) 115126 (8 pp). DOI: 10.1103/PhysRevB.79.115126.
- [34] V.L. Bonch-Bruevich, S.G. Kalashnikov, Physics of Semiconductors, Nauka, Moscow, 1977.

Figure Captions

Fig. 1. Temperature dependence of the resistivity of the investigated CZTS films. Top panel: as-grown samples; middle – annealed with thermal treatment TT1; bottom – annealed at different conditions for the sample S1. Inset: Plot of $\ln \rho$ vs. $1/T$ for samples S1-1 and S2-1 (shifted by 3 Ω cm for convenience).

Fig. 2. Grazing incidence X-ray diffraction of the sample S1 before and after different thermal treatments. JCPDS files of CZTS and Cu_2S compounds are shown as references.

Fig. 3. Schematic representation of the DOS in the acceptor band near the edge of the valence band, E_v for (a) as-grown samples and S3-1 and (b) for samples S1-1 and S2-1. The intervals of the localized states are hatched.

Fig. 4. The plots of $\ln (\rho / T^{1/4})$ vs. $T^{-1/4}$ in the investigated CZTS films. Top panel – as-grown samples; bottom – annealed samples by using TT1 thermal treatment. Some plots are shifted along the vertical axis for convenience. Straight lines are linear fits.

Table 1. Growth process conditions and composition of the CZTS thin films. The composition of the samples was measured by EDX.

Sample	Flash evaporation	TT	Cu (at%)	Sn (at%)	Zn (at%)	S (at%)	Cu/(Sn+Zn)	Zn/Sn	S/M
S1	$T_{\text{crucible}} = 1100^{\circ}\text{C}$, +20 % excess ZnS	-	22.26	11.63	13.96	52.15	0.87	1.20	1.09
		1	21.64	12.14	13.52	53.25	0.82	1.11	1.14
		2	24.21	8.02	16.89	50.87	0.97	2.12	1.04
		3	21.97	11.81	14.24	51.97	0.84	1.21	1.08
S2	$T_{\text{crucible}} = 1100^{\circ}\text{C}$, +10 % excess ZnS	-	22.55	14.65	11.45	51.36	0.87	0.78	1.06
		1	22.11	12.43	11.05	54.41	0.94	0.89	1.19
S3	$T_{\text{crucible}} = 1075^{\circ}\text{C}$, +20 % excess ZnS	-	25.29	9.31	14.99	50.40	1.04	1.62	1.02
		1	23.97	10.50	13.00	52.54	1.02	1.24	1.11

TT = thermal treatment. TT1: $T = 600^{\circ}\text{C}$, 1000 Pa, 21°C/min , 30 min

TT2: $T = 600^{\circ}\text{C}$, 100 Pa, 21°C/min , 30 min

TT3: $T = 550^{\circ}\text{C}$, 100 Pa, 10°C/min , 30 min

Table 2. The temperature borders of the VRH conduction (T_v and T_m), the characteristic VRH temperature (T_0), the prefactor VRH constant (A), the width of the acceptor band (W), the relative acceptor concentration (N/N_c) and the relative values of the localization radius (a/a_0 and a/a_B), the mobility edge (E_c) and the DOS g (μ).

Sample	T_v	T_m	T_0	A	W	N/N_c	a/a_0	a/a_B	E_c	g (μ)
No.	(K)	(K)	(K)	($\Omega \text{ cm K}^{-1/4}$)	(meV)				(meV)	($10^{17} \text{ meV}^{-1} \text{ cm}^{-3}$)
S1	220	150	1.81×10^4	2.08×10^{-3}	28	0.75	4.0	4.2	22	2.4
S2	260	180	8.88×10^2	3.41×10^{-3}	15	0.88	8.5	8.5	13	5.3
S3	215	140	5.65×10^4	2.93×10^{-5}	37	0.68	3.1	3.0	25	1.7
S1-1*	145	67	1.79×10^7	1.94×10^{-7}	117	0.13	—	—	—	—
S2-1*	177	76	2.01×10^7	8.61×10^{-8}	140	0.14	—	—	—	—
S3-1*	123	31	7.05×10^5	3.32×10^{-4}	46	0.41	1.7	1.7	19	0.8

* S1, S2 and S3 samples after TT1.

Figure 1

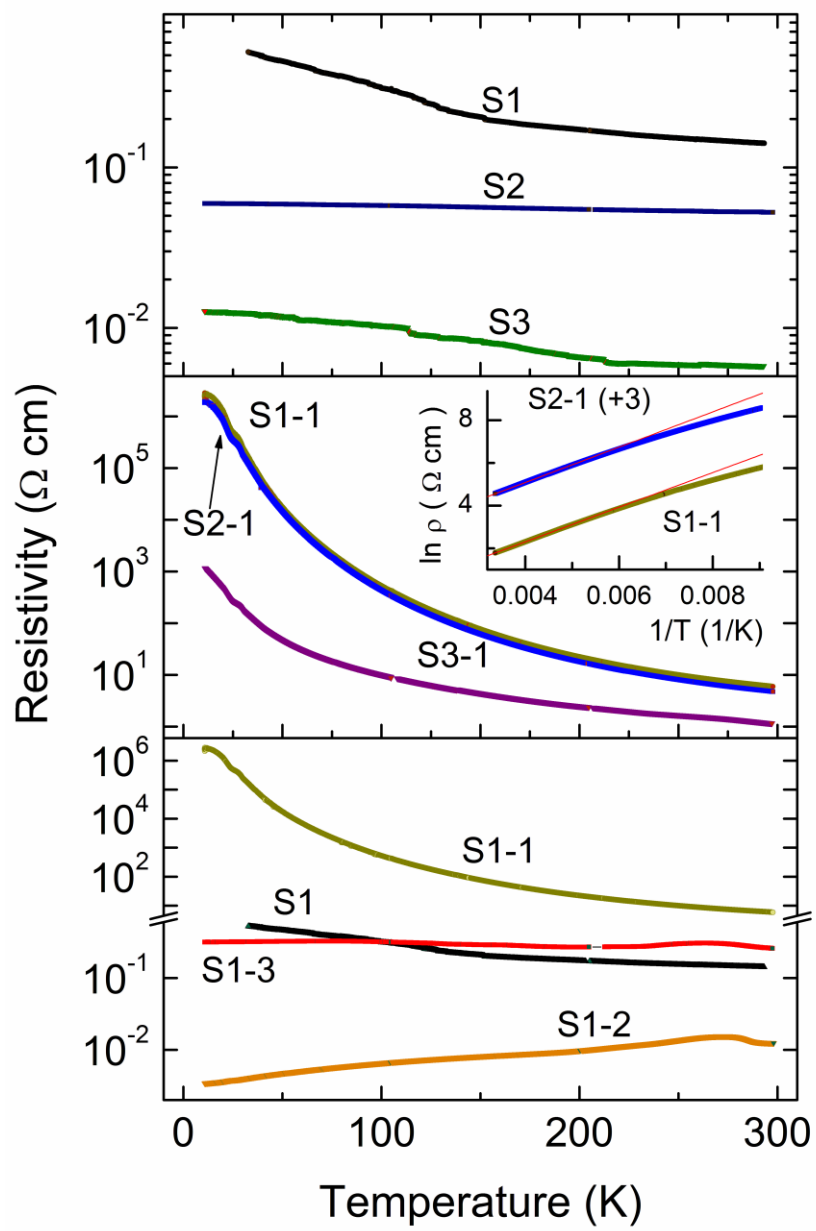


Figure 2

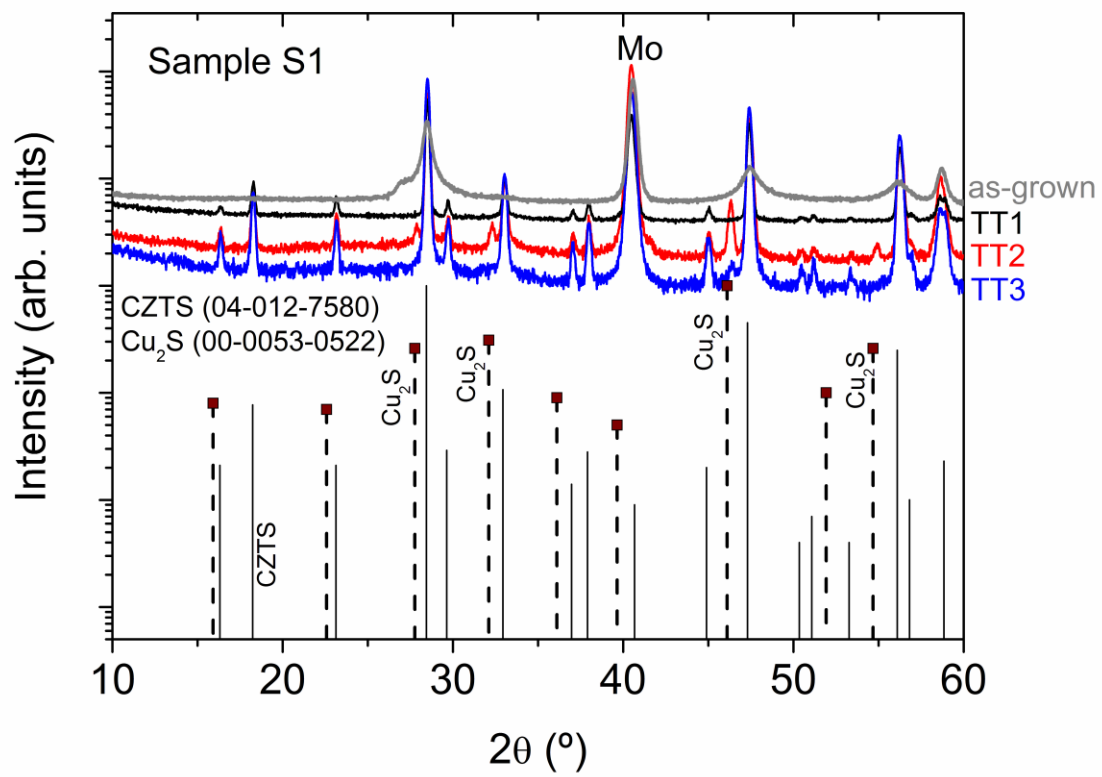


Figure 3

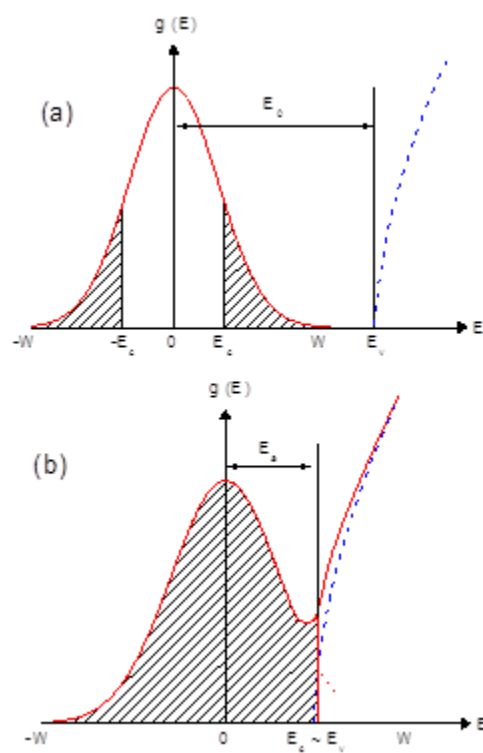


Figure 4

